Accuracy Assessment of UAV Photogrammetry System with RTK Measurements for Direct Georeferencing

Zhuangqun Niu [1], Hui Xia [3, 4], Pengjie Tao [1, 2], Tao Ke [1, 2, *]

[1] School of Remote Sensing and Information Engineering, Wuhan University, Wuhan 430079, China – niuzhuangqun@whu.edu.cn, pjtao@whu.edu.cn, ketao@whu.edu.cn
[2] Hubei Luojia Laboratory, Wuhan 430079, China
[3] Changjiang Spatial Information Technology Engineering Co., Ltd., Wuhan 430010, China - xiahui3@cjwsjy.com.cn
[4] Changjiang Design Group Co., Ltd., Wuhan 430010, China

Keywords: UAV photogrammetry, RTK, Accuracy assessment, Direct georeferencing.

Abstract

The direct georeferencing accuracy of unmanned aerial vehicle (UAV) images with real-time kinematic (RTK) measurements is a concerned topic in the community of photogrammetry. This study assesses the capabilities of a multi-rotor platform equipped with RTK technology, specifically a DJI Phantom 4 RTK UAV, for robust direct georeferencing. The UAV surveyed a square and a building at Wuhan University to assess the accuracy and spatial consistency of direct georeferencing in close-range photography. We tested checkpoint errors under various ground control points (GCPs) configurations. The results show that without GCP, an analysis of 71 spatially distributed checkpoints produced a root mean square error (RMSE) of 5.58 cm in the Z direction. This finding indicates that RTK-equipped UAVs can achieve acceptable error margins even without using GCPs, thereby fulfilling the precision requirements for large-scale mapping.

1. Introduction

Unmanned Aerial Vehicle (UAV) photogrammetry, has emerged as a pivotal innovation in remote sensing, offering advantages such as compact size, cost-effectiveness, high-resolution imaging, flexible deployment, and ease of operation (Tomaštík et al., 2019). These benefits have positioned UAV photogrammetry as a practical alternative to traditional aerial photogrammetry (Remondino et al., 2012), revolutionizing terrain mapping especially when combined with Structure from Motion (SfM) technology (Martínez-Carricondo et al., 2018). This synergy enhances the acquisition of accurate and cost-efficient 3D spatial data, enabling the efficient generation of digital surface models (DSMs), digital elevation models (DEMs), and digital orthophoto maps (DOMs). Consequently, UAV photogrammetry has been extensive applied across various fields including infrastructure monitoring (Greenwood et al., 2019), disaster emergency (Fazeli et al., 2016), terrain modelling (Senkal et al., 2021), precision agriculture (Moghimi et al., 2020), archaeological documentation (Lin et al., 2019), and cadastral surveying (Barry and Coakley, 2013). These widespread adoptions underscore the transformative impact of UAV photogrammetry in both research and practical applications.

Despite its advancements, UAV photogrammetry initially faced challenges due to the inferior capability of onboard sensors compared to professional-grade sensors in manned systems. This limitation necessitated extensive ground control efforts to achieve the desired accuracy (Gerke and Przybilla, 2016), increasing workload and costs, and thereby restricting the full potential of UAVs in the mapping industry. However, recent technological advancements, particularly the maturation and subsequent cost reduction of real-time kinematic (RTK) technology, have begun to address these limitations. Consumer-grade RTK positioning devices, now suitable for integration, have made precise, real-time, three-dimensional positioning affordable and accessible (Stempfhuber and Buchholz, 2012). The integration of RTK devices and the synergy SfM direct georeferencing method in UAVs, exemplified by the DJI Phantom 4 RTK, has streamlined photogrammetry workflows, reducing reliance on ground control points (GCPs). This advancement not only reduces the cost and simplifies field investigation work but also expands the potential applications of UAV photogrammetry to areas previously deemed inaccessible or too challenging for traditional methods (BUĞDAY, 2018; Tur et al., 2020).

Nevertheless, given the complexity of photogrammetry pipeline, verifying the positional accuracy of the acquired images and the georeferencing outcomes remains imperative (Rangel et al., 2018). Previous literatures have contributed valuable insights. Taddia et al. (2020) explored the accuracy of 3D models and digital terrain models (DTMs) generated using direct georeferencing in coastal areas, finding comparable results with and without GCPs in oblique image datasets. Gerke and Przybilla (2016) investigated cross-flight effects at various altitudes with a fixed-wing drone equipped with RTK, observing a significant reduction in block deformation and improved accuracy in flat areas. Zeybek (2021) compared the accuracy of network-based continuously operating reference stations (i.e. network RTK) and differential-based real-time kinematic (D-RTK), with both methods achieving high levels of horizontal and vertical accuracy. Varbla et al. (2021) assessed the accuracy of UAV equipped with RTK technology in conducting as-built surveys, finding that the accuracy of direct georeferencing could rival ground laser scanning. Stroner et al. (2020) examined the accuracy of the DJI Phantom 4 RTK system in urban and rural areas with different georeferencing configurations, they found that RTK method provided expected level of accuracy of 1–2 ground sampling distance (GSD) for both the vertical and horizontal directions. Stott et al. (2020) conducted a study on oblique image using the DJI Phantom 4 RTK, which revealed the impact of different GCP configurations on checkpoint accuracy in riverine environments. Their results imply that DJI Phantom 4 RTK can produce acceptable errors without GCPs and no vertical systematic errors.

---

* Corresponding author

However, these studies predominantly focused on data collected at higher flight heights and did not investigate the spatial consistency of outputs using direct georeferencing. This research gap presents an opportunity for this study to conduct experiments under these specific conditions, adding a new dimension to the understanding of UAV photogrammetry's capabilities and limitations.

2. Materials and Method

2.1 Study areas

To accurately evaluate the precision of direct georeferencing using RTK technology, an elaborate study area was designated within Youyi Square, located at Wuhan University. This location was chosen for its diverse terrain features, including granite floors, asphalt pavements, grassland, and tree-covered areas, covering a total area of 180 m by 180 m. At the center of this area lies a platform, which is about 42 m in length, 30 m in width, as depicted in Figure 1(a). Through the use of a total station, a comprehensive measurement of 71 checkpoints was conducted across the area, achieving a positional accuracy less than 0.5 cm, depicted in Figure 1(b).

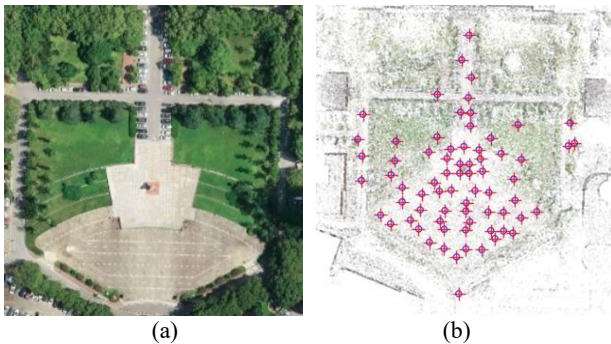<table>
<tr><td>(a)</td><td>(b)</td></tr>
</table>

Figure 1. (a) Overview of area 1; (b) distribution of ground checkpoints.

In addition, to further evaluate the spatial consistency of direct georeferencing, the Teaching and Experimental Building, situated 20 meters east of the area 1, was selected as a secondary study area. This high-rise structure, depicted in Figure 2, provides a contrasting backdrop for additional validation efforts. Eight pairs of symmetric points on the northern and southern façades of this building were identified to assess the spatial consistency accuracy. The distribution of these points on the southern façade is illustrated in Figure 2(b). The incorporation of these two distinct locations, played a crucial role in facilitating a comprehensive evaluation of the UAV system's georeferencing capabilities under varied environmental conditions.
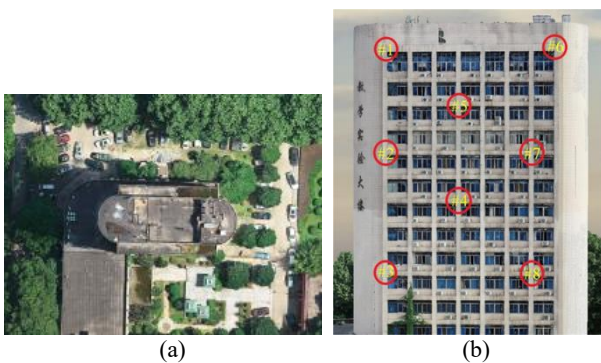

Figure 2. (a) Overview of area 2; (b) distribution of the identified points on the southern facade of the building.

2.2 UAV platform

In this study, the DJI Phantom 4 RTK UAV was selected for experiments. This UAV is equipped with a gimbal, offering a pitch angle range of -90 to +30 degrees, and features a wide-angle camera with 20 million effective pixels and an equivalent focal length of 24 mm, making it highly suitable for capturing high-resolution multi-view images. A pivotal feature of this UAV is its support for both single-frequency and multi-frequency global navigation satellite system (GNSS) positioning, enabling centimeter-level precision in determining UAV's location through either network RTK or a high-precision GNSS mobile station—capabilities that align closely with the requirements of this study. Additionally, the DJI Phantom 4 RTK is capable of recording GNSS observational data in RINEX format onto a memory card during the image acquisition process. This feature allows for precise UAV location positioning via Post-Processing Kinematic (PPK) technology. For the purposes of our experiments, network RTK was utilized to geotag the images. The UAV's detailed technical specifications and capabilities are thoroughly enumerated in Table 1, offering a comprehensive overview of the equipment used in this research.

Modules	Specifications
Aircraft	350 mm wheelbase 4-rotor unmanned aerial vehicle
Max Flight Time	Approx. 30 minutes
Max Speed	Horizontal 14m/s, vertical 6m/s
Max Service Ceiling Above Sea Level	19685 ft (6000 m)
GNSS	Single-Frequency and Multi-Frequency GNSS
Sensor	1" CMOS; Effective pixels: 20 M
Lens	FOV 84°; 8.8 mm / 24 mm (35 mm format equivalent:24 mm); f/2.8 - f/11
Max Image Size	4864×3648 (4:3) 5472×3648 (3:2)
Mechanical Shutter Speed	8 - 1/2000 s
ISO Range	Photo:100-3200 (Auto) 100-12800 (Manual)
Measuring Frequency	Forward/Rear: 10 HZ; Downward: 20 HZ
Gimbal	3-axis (tilt, roll, yaw); Angular Vibration Range: ±0.02°; Pitch: -90° to +30°

Table 1. Specifications of DJI Phantom 4 RTK UAV.

2.3 Data collection

In Area 1, the UAV data acquisition executed according to a meticulously planned flight strategy. The UAV navigated an east-west trajectory at a consistent altitude of 35 meters, following a serpentine path to ensure maximal coverage and comprehensive data collection across the designated area. During the photography sessions, the camera's pitch angle, φ, was set to -90° for conventional nadir photography and adjusted to -45° for oblique photography, thereby capturing a variety of terrain perspectives. A total of 1059 images were captured under these settings, comprising 683 nadir images and 376 oblique images, respectively. The detailed flight path is illustrated in Figure 3. The density of this flight path resulted in an overlap of

80% between successive flight strips, eliminating the need for additional north-south oriented flights.

Figure 3. The flight path over area 1.

In Area 2, the UAV was tailored to capture the building's facades from a 15 m distance. The flight trajectories, as shown in Figure 4(a), were designed with the camera's principal axis perpendicular to the building's facade. The dense tree coverage at the building's northern side posed significant challenges to the flight planning, resulting in seven flight lines for frontal-parallel photography on this side, as opposed to eight flight lines on the more accessible southern side. To ensure more thorough coverage, additional flights were added, by offsetting the camera's principal axis 20 degrees horizontally at same shooting location, emulating oblique photography, yielding a rich dataset of 485 images. It is important to note that flights were not conducted along the eastern and western sides of the building to focus on assessing the spatial consistency of direct georeferencing. As a result, only minimal image overlap is observed on these building sides, as detailed in Figure 4(b).
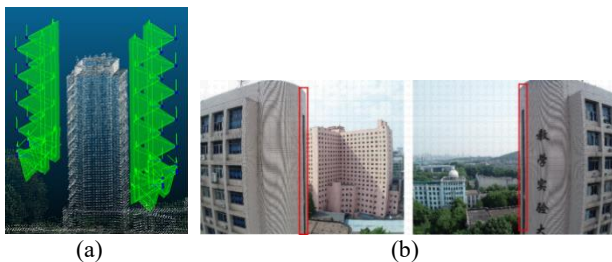

(a)   (b)

Figure 4. (a) The trajectory of the UAV along the facades of the building; (b) limited image overlap, outlined in red rectangle.

2.4 Method

In this study, the interior orientation parameters were consistently estimated utilizing the self-calibration SfM approach, with the pinhole camera model serving as the imaging model, The formula is presented as follows:

$$x - c_x + \Delta x = -f \frac{r_{11}(X - X_S) + r_{21}(Y - Y_S) + r_{31}(Z - Z_S)}{r_{13}(X - X_S) + r_{23}(Y - Y_S) + r_{33}(Z - Z_S)}$$
$$y - c_y + \Delta y = -f \frac{r_{12}(X - X_S) + r_{22}(Y - Y_S) + r_{32}(Z - Z_S)}{r_{13}(X - X_S) + r_{23}(Y - Y_S) + r_{33}(Z - Z_S)}$$
(1)

Where, x and y are the image pixel coordinates, X, Y and Z are the world coordinates of the target points, r_{ij} represents the elements of the camera's 3×3 rotation matrix, X_S, Y_S and Z_S denote the world coordinates of camera, the principal distance is given by f, while c_x and c_y are the principal point on the image plane. The terms Δx and Δy account for lens distortion.

Lens distortion is modeled using the radial-tangential distortion model, detailed in Equation (2):

$$\Delta x = x'(k_1 r^2 + k_2 r^4 + k_3 r^6) + 2p_1 x' y' + p_2(r^2 + 2x'^2)$$
$$\Delta y = y'(k_1 r^2 + k_2 r^4 + k_3 r^6) + 2p_2 x' y' + p_1(r^2 + 2y'^2)$$
(2)

Where, $x' = x - c_x$, $y' = y - c_y$ with $r^2 = x'^2 + y'^2$ representing the squared distance from the pixel to the principal point. The distortion parameters to be determined are k_1, k_2, k_3 (radial distortion parameters), and p_1, p_2 (tangential distortion parameters).

2.5 Data processing

To ensure the comparability of experimental results, this study employed Agisoft Metashape, a widely used software, for SfM processing. All images' geographic coordinates were converted from the WGS 84 coordinate system to the WGS 84 / UTM zone 50N format, ensuring alignment with the projected coordinate system used in our analysis. For georeferencing procedures, default configurations within Agisoft Metashape were applied.

In Area 1, to evaluate the accuracy of direct georeferencing and assess the effect of oblique image, data were categorized into three groups: nadir, oblique, and a mixture set of nadir and oblique images. For each group, three types of geometrical constraints were applied: utilization of RTK positioning alone, GCPs alone, and a hybrid approach employing both RTK positioning and GCPs. To further investigate the impact of varying numbers and distributions of GCPs on georeferencing accuracy, all images retained their RTK positioning data for analysis under different GCP configurations. The accuracy parameters for RTK and GCPs were established at 0.1 meters and 0.005 meters, respectively.

Contrastingly, Area 2 was exclusively focused on evaluating the stability and reliability of direct georeferencing using RTK information alone. Eight pairs of points located on the northern and southern facades of the building were selected as evaluation points. This focus was driven by the necessity to determine RTK's effectiveness in scenarios where employing ground control is not feasible or practical. By confining the control data to RTK for the camera alignment, our objective was to meticulously assess RTK's capacity to sustain both stability and accuracy in photogrammetric applications. Aside from the distinct considerations outlined above, all processing settings for Area 2 remained consistent with those applied in Area 1.

3. Results and discussion

3.1 Results

The overall accuracy assessment was initiated based on the residual errors computed at the checkpoints (CPs). All GCPs and checkpoints were annotated on the images following the standard photogrammetry procedure. To evaluate the

georeferencing accuracy, the root mean square errors (RMSEs) were calculated in the X, Y, and Z directions, as well as on the plane, as determined using the following equations:

$$RMSE(X) = \sqrt{\frac{\sum_{i=1}^{n}(X_i^{est.} - X_i^{CP})^2}{n}}$$

$$RMSE(Y) = \sqrt{\frac{\sum_{i=1}^{n}(Y_i^{est.} - Y_i^{CP})^2}{n}}$$

$$RMSE(Z) = \sqrt{\frac{\sum_{i=1}^{n}(Z_i^{est.} - Z_i^{CP})^2}{n}}$$

$$(3)$$

$$RMSE(XY) = \sqrt{\frac{\sum_{i=1}^{n}[(X_i^{est.} - X_i^{CP})^2 + (Y_i^{est.} - Y_i^{CP})^2]}{n}}$$

Where $X_i^{est.}$, $Y_i^{est.}$, $Z_i^{est.}$ represent the estimated coordinates of the checkpoints, X_i^{CP}, Y_i^{CP}, Z_i^{CP} denote the measured ground truth coordinates of the checkpoints. $RMSE(X)$, $RMSE(Y)$ and $RMSE(Z)$ quantify the RMSE in the respective directions, with $RMSE(XY)$ representing the horizontal RMSE.

3.1.1 Area 1

The outcomes of the various processing configurations are presented in Table 2. Configurations (1) through (7) are aimed at evaluating the impact of oblique image and RTK data on direct georeferencing accuracy, In contrast, configurations (10) through (14) delve into the effects of oblique image and different GCP configurations on georeferencing accuracy when incorporating RTK data.

The arrangement of GCPs within these distinct configurations is depicted in Figure 5. Visualization of the results is depicted in Figures 6 and 7. Specifically Figure 6 details the residual errors for GCPs and checkpoints across various configurations, offering insight into the achieved spatial accuracy. Concurrently, Figure 7 illustrates the distributions of residual errors of image positions under these different configurations, further highlighting the georeferencing precision within the study areas.

ID	Configuration	RMSEs of checkpoints (cm)			
		X	Y	XY	Z
(1)	N+RTK	1.81	1.75	2.52	22.97
(2)	O+RTK	1.46	2.52	2.92	4.31
(3)	N+O+RTK	1.26	0.88	1.54	5.58
(4)	N+4GCPs	1.20	0.88	1.49	11.51
(5)	O+4GCPs	1.72	1.35	2.19	1.07
(6)	N+O+4GCPs	1.26	1.05	1.64	1.06
(7)	N+RTK+4GCPs	1.08	0.91	1.41	1.15
(8)	O+RTK+4GCPs	1.49	1.32	1.99	1.37
(9)	N+O+RTK+4GCPs	1.03	1.03	1.45	1.74
(10)	N+RTK+1GCP	1.42	1.14	1.82	3.08
(11)	N+RTK+1GCP*	1.61	1.35	2.10	2.65
(12)	N+O+RTK+1GCP	1.25	1.75	2.15	4.83
(13)	N+O+RTK+1GCP*	1.56	1.19	1.96	3.23
(14)	N+O+RTK+9GCPs	1.04	1.01	1.45	0.90

'N' represents nadir images, 'O' denotes oblique images, and 'N+O' signifies a combination of them.

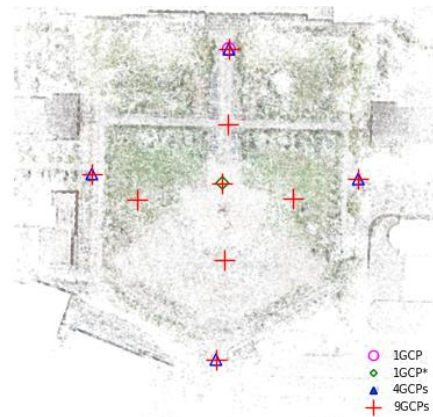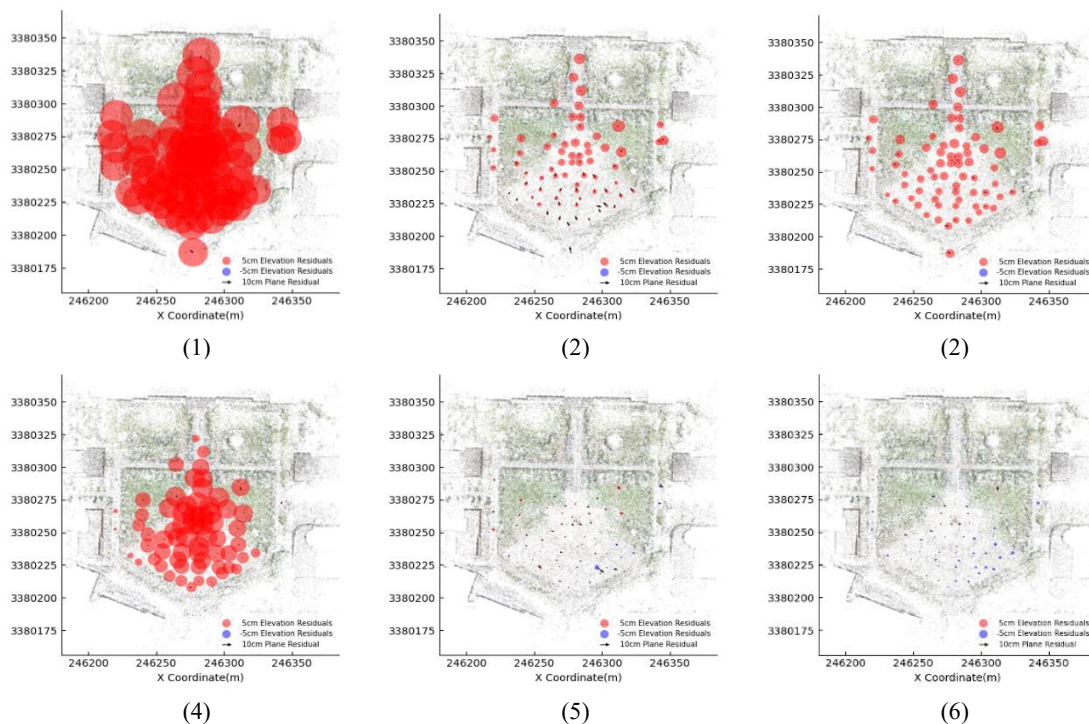Table 2. The RMSEs of checkpoints associated with different processing configurations.

Figure 5. The arrangement of GCPs within these distinct configurations.

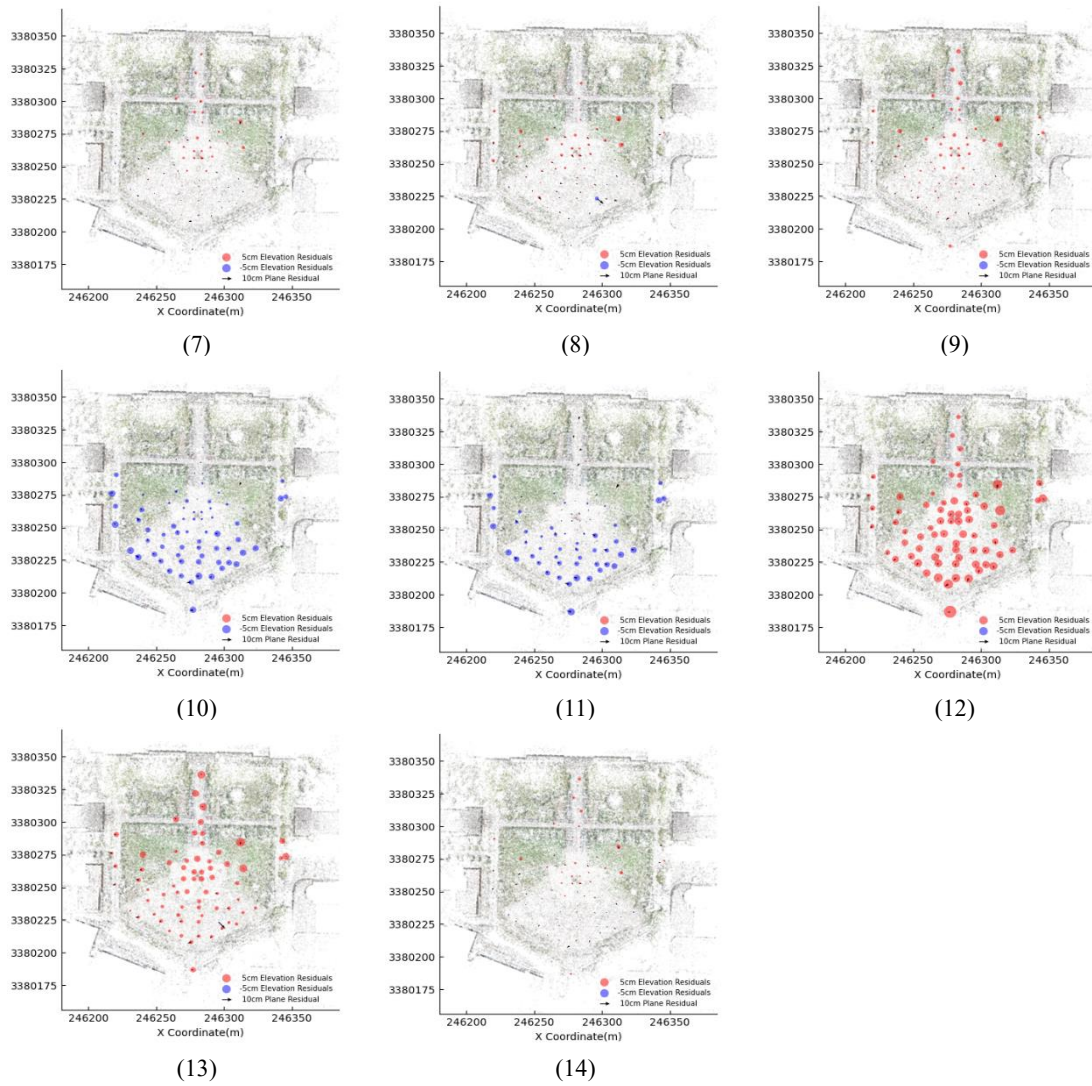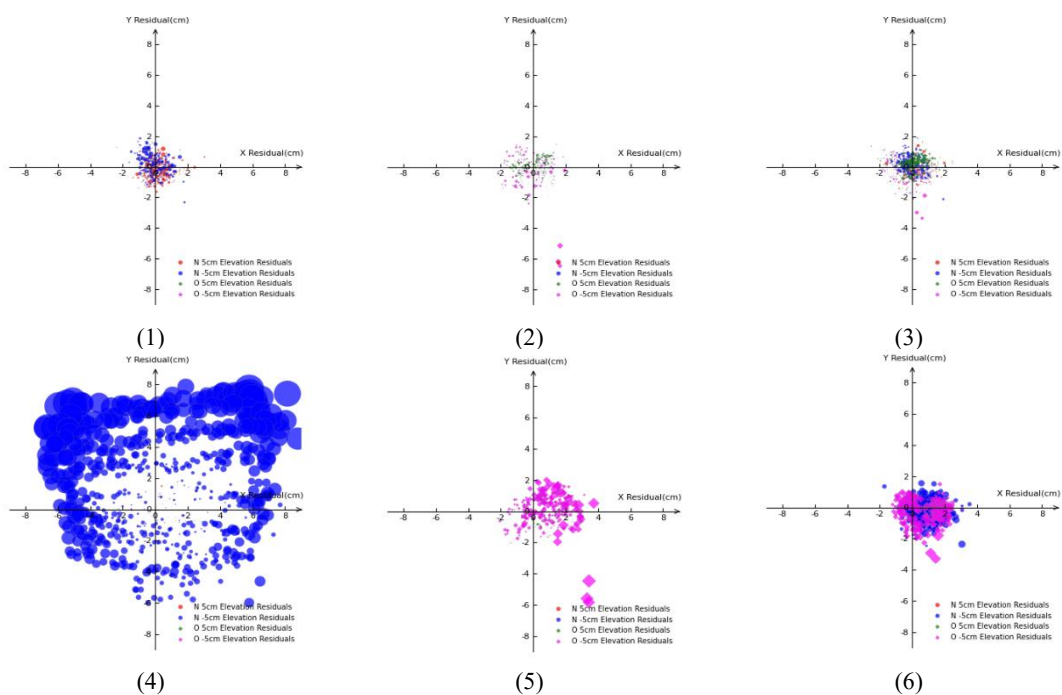(1)

(2)

(2)

(4)

(5)

(6)

Figure 6. The residual error distribution of GCPs and checkpoints under different configurations.
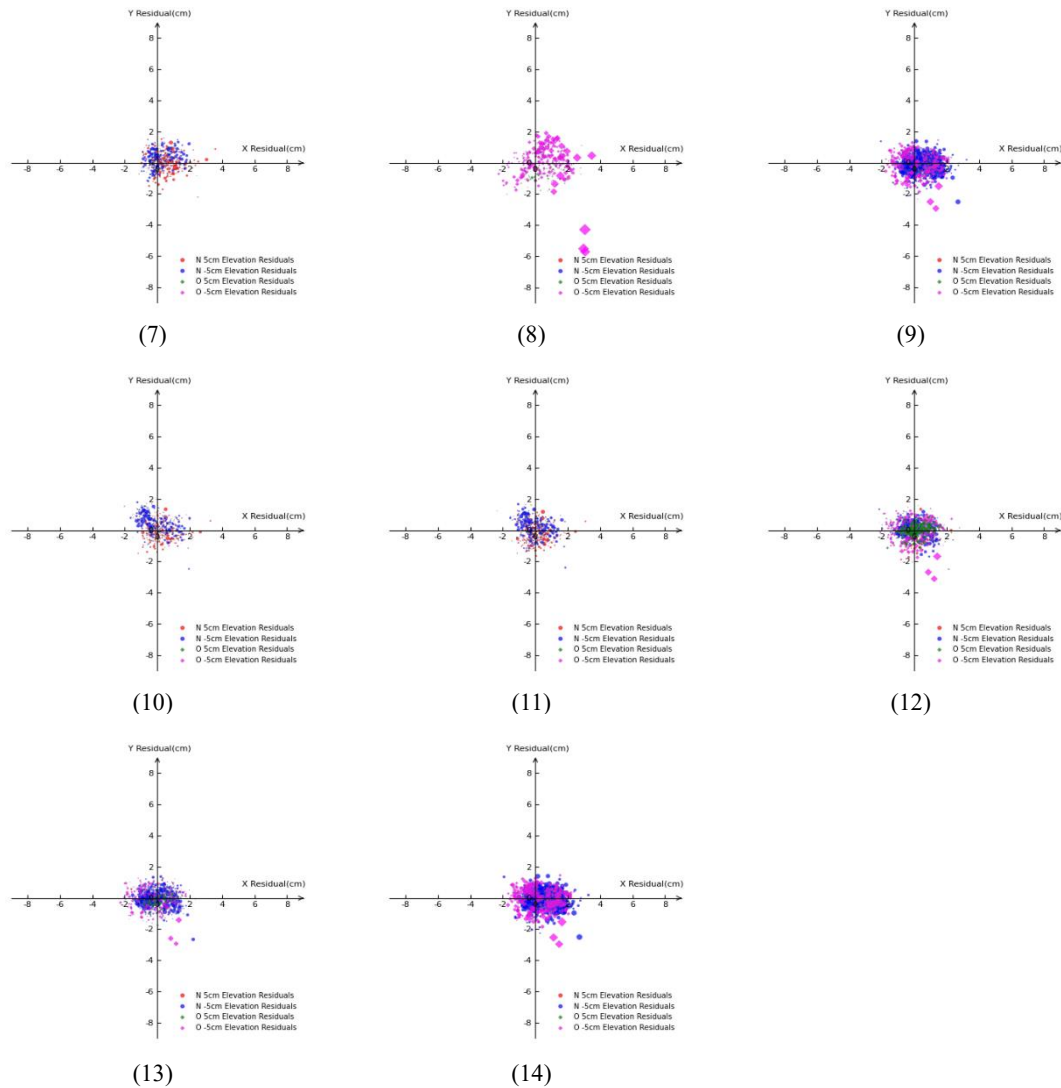
Figure 7. The residual error of image positions under different configurations.

3.1.2 Area 2

Figure 8 presents the results of direct georeferencing for the building, with the corresponding statistical analysis outlined in Table 3. This analysis measures the coordinate differences at specified points, thereby enabling an assessment of the spatial consistency accuracy in the UAV's direct georeferencing.
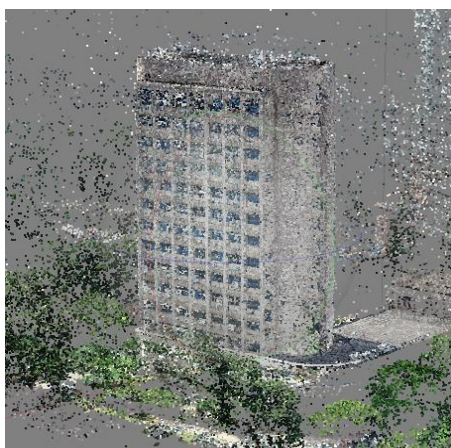

Figure 8. The direct georeferencing result of the building.

ID	ΔX(m)	ΔY(m)	ΔZ(m)
#1	-0.48	-17.91	0.04
#2	-0.47	-17.94	0.07
#3	-0.45	-17.94	0.08
#4	-0.46	-17.93	0.09
#5	-0.48	-17.93	0.05
#6	-0.48	-17.91	0.05
#7	-0.47	-17.93	0.04
#8	-0.47	-17.92	0.08
Mean	-0.47	-17.93	0.06
Standard deviation	0.01	0.01	0.02

Table 3. Statistical results of coordinate differences at symmetrical points to assess the spatial consistency accuracy on the northern and southern façades of the building.

3.2 Discussion

3.2.1 Area 1

By comparing configurations (1), (2), and (3) in Table 2, it is evident that relying solely on nadir images, when using only RTK for direct georeferencing, results in significant vertical errors. This could be due to the incorrect focal length estimation during self-calibration (Forlani et al., 2018). Using only oblique

images reduces the vertical error to a reasonable range, but increases the horizontal error. Combining both types of images can achieve an optimal outcome. And, for all three groups, the horizontal direct georeferencing accuracy remains within 5 cm, and the vertical accuracy for 'O' and 'N+O' approaches the 5 cm mark.

When using only a small number of GCPs, results from configurations (4), (5), and (6) in Table 2 exhibit similar trends to those observed when RTK is used exclusively. As shown in Figure 6, configuration (4) exhibits significantly larger residual errors in image positions, despite the relatively small horizontal RMSE of the checkpoints, indicating a suboptimal georeferencing outcome. However, the inclusion of oblique images significantly enhances the results, as demonstrated by configuration (6), highlighting the importance of incorporating oblique images in self-calibration SfM approach, when GCPs are the only available references.

When using both of RTK and GCPs, configurations (7), (8), and (9) present slightly different outcomes. Although all three configurations show similar levels of accuracy, the configuration using only nadir images performs best, followed by the one using only oblique images, and the combination of both yields the lowest accuracy. This outcome suggests that the SfM algorithm may achieve adequate estimates when both GCPs and RTK are available. However, in configurations using only oblique images, the oblique nature of the images increases the matching difficulty, subsequently leading to reduced estimation accuracy. Furthermore, in the combined configuration, the constraint effect of GCPs may be weakened as the number of observations increases. Examining configuration (14), it becomes evident that further increasing the number of GCPs leads to the highest level of accuracy.

In the case of using RTK data, the comparison between configurations (1), (10), (11), and (7) reveals that, by solely utilizing nadir images and adding a small number of GCPs, the accuracy can be significantly improved. Moreover, the more evenly distributed the GCPs are, the higher the accuracy tends to be. Comparing configurations (10), (12), (11), (13) reinforces the previous finding that, when using RTK data and a small amount of GCPs, the addition of oblique image may decrease the precision of the results. However, the resulting differences still fall within an acceptable range. Given the crucial role of oblique images in subsequent 3D reconstruction, their inclusion remains a prudent decision.

3.2.2 Area 2

The challenge in this experiment lies in the absence of GCPs and the reliance on the RTK positioning accuracy. If the RTK positioning is imprecise, it is expected that the consistency of the northern and southern sides will remain non-aligned. This is due to the insufficient overlap and lack of external reference points to align the models accurately. Conversely, if the RTK positioning is precise, it would enable the accurate alignment, demonstrating the effectiveness of high-accuracy RTK in UAV photogrammetry. Such an outcome would signify a significant advancement in the capability of RTK systems to produce coherent models in situations with limited photographic overlap and no GCPs.

Upon precise measurement of symmetrically specified points, a notable mean elevation difference of 6.3 cm was observed across the building's sides. Such a level of discrepancy is critical to note as it reflects the elevation accuracy achievable in our direct georeferencing process. In terms of horizontal alignment, the models demonstrated greater precision, evidenced by a standard deviation of only 1 cm. However, significant discrepancies were observed in the X and Y directions, with differences of 47 cm and 17.93 m, respectively. One contributing factor to these differences is the building's orientation; which is not perfectly aligned with the east-west direction. The larger discrepancy observed in the Y direction can be attributed to the fact that it corresponds to the building's width.

4. Conclusion

This study was dedicated to assessing the accuracy and spatial consistency of direct georeferencing based on RTK technology. Our findings indicate that the DJI Phantom 4 RTK achieves remarkable photogrammetric precision, particularly in the horizontal plane. A horizontal accuracy of 1-3 cm and vertical accuracy of 4-6 cm were achieved, using direct georeferencing method without employing GCPs. However, some systematic errors may occur in the vertical direction, suggesting the potential need for GCPs in applications requiring precise vertical accuracy, such as detailed topographic mapping.

From our experiments, we can draw the following conclusions: (1) The DJI Phantom 4 RTK demonstrates exceptional precision in recording exposure positions, a crucial factor for accurate direct georeferencing. (2) The UAV's photogrammetric measurement system demonstrates spatial consistency, thereby ensuring reliability across different data collection scenarios. (3) A discrepancy between vertical and horizontal accuracy indicates potential systematic errors in elevation measurements, requiring further examination. (4) Integrating nadir and oblique images enhances positioning accuracy, especially in complex photogrammetric tasks, by providing a more comprehensive perspective of the surveyed area.

References

Barry, P., and Coakley, R., 2013. Accuracy of UAV Photogrammetry Compared with Network RTK GPS. *Int. Arch. Photogramm. Remote Sens* 2:2731.

BUĞDAY, E., 2018. Capabilities of Using UAVs in Forest Road Construction Activities. *European Journal of Forest Engineering* 4(2):56–62.

Fazeli, H., Samadzadegan, F., and Dadrasjavan, F., 2016. Evaluating the Potential of RTK-UAV for Automatic Point Cloud Generation in 3D Rapid Mapping. *The International Archives of the Photogrammetry, Remote Sensing and Spatial Information Sciences* 41:221–226.

Forlani, G., Dall'Asta, E., Diotri, F., Morra di Cella, U., Roncella, R., and Santise, M., 2018. Quality Assessment of DSMs Produced from UAV Flights Georeferenced with On-Board RTK Positioning. *Remote Sensing* 10(2):311.

Gerke, M., and Przybilla, H.-J., 2016. Accuracy Analysis of Photogrammetric UAV Image Blocks: Influence of Onboard RTK-GNSS and Cross Flight Patterns. *Photogrammetrie, Fernerkundung, Geoinformation* (1):17–30.

Greenwood, W.W., Lynch, J.P., and Zekkos, D., 2019. Applications of UAVs in Civil Infrastructure. *Journal of Infrastructure Systems* 25(2):04019002.

Lin, Y.-C., Cheng, Y.-T., Zhou, T., Ravi, R., Hasheminasab, S.M., Flatt, J.E., Troy, C., and Habib, A., 2019. Evaluation of UAV LiDAR for Mapping Coastal Environments. *Remote Sensing* 11(24):2893.

Martínez-Carricondo, P., Agüera-Vega, F., Carvajal-Ramírez, F., Mesas-Carrascosa, F.-J., García-Ferrer, A., and Pérez-Porras, F.-J., 2018. Assessment of UAV-Photogrammetric Mapping Accuracy Based on Variation of Ground Control Points. *International Journal of Applied Earth Observation and Geoinformation* 72:1–10.

Moghimi, A., Yang, C., and Anderson, J.A., 2020. Aerial Hyperspectral Imagery and Deep Neural Networks for High-Throughput Yield Phenotyping in Wheat. *Computers and Electronics in Agriculture* 172:105299.

Rangel, J.M.G., Gonçalves, G.R., and Pérez, J.A., 2018. The Impact of Number and Spatial Distribution of GCPs on the Positional Accuracy of Geospatial Products Derived from Low-Cost UASs. *International Journal of Remote Sensing* 39(21):7154–7171.

Remondino, F., Barazzetti, L., Nex, F., Scaioni, M., and Sarazzi, D., 2012. UAV Photogrammetry for Mapping and 3d Modeling–Current Status and Future Perspectives. *The International Archives of the Photogrammetry, Remote Sensing and Spatial Information Sciences* 38:25–31.

Senkal, E., Kaplan, G., and Avdan, U., 2021. Accuracy Assessment of Digital Surface Models from Unmanned Aerial Vehicles' Imagery on Archaeological Sites. *International Journal of Engineering and Geosciences* 6(2):81–89.

Stempfhuber, W., and Buchholz, M., 2012. A Precise, Low-Cost RTK GNSS System for UAV Applications. *The International Archives of the Photogrammetry, Remote Sensing and Spatial Information Sciences* 38:289–293.

Stott, E., Williams, R.D., and Hoey, T.B., 2020. Ground Control Point Distribution for Accurate Kilometre-Scale Topographic Mapping Using an RTK-GNSS Unmanned Aerial Vehicle and SfM Photogrammetry. *Drones* 4(3):55.

Štroner, M., Urban, R., Reindl, T., Seidl, J., and Brouček, J., 2020. Evaluation of the Georeferencing Accuracy of a Photogrammetric Model Using a Quadrocopter with Onboard GNSS RTK. *Sensors* 20(8):2318.

Taddia, Y., Stecchi, F., and Pellegrinelli, A., 2020. Coastal Mapping Using DJI Phantom 4 RTK in Post-Processing Kinematic Mode. *Drones* 4(2):9.

Tomaštík, J., Mokroš, M., Surový, P., Grznárová, A., and Merganič, J., 2019. UAV RTK/PPK Method—an Optimal Solution for Mapping Inaccessible Forested Areas? *Remote Sensing* 11(6):721.

Tur, R., Uzunsakal, L., and Mehr, A.D., 2020. Coastline Change Determination Using UAV Technology: A Case Study along the Konyaaltı Coast, Antalya, Turkey. *Drones in Smart-Cities* 123–141.

Varbla, S., Puust, R., and Ellmann, A., 2021. Accuracy Assessment of RTK-GNSS Equipped UAV Conducted as-Built Surveys for Construction Site Modelling. *Survey Review* 53(381):477–492.

Zeybek, M., 2021. Accuracy Assessment of Direct Georeferencing UAV Images with Onboard Global Navigation Satellite System and Comparison of CORS/RTK Surveying Methods. *Measurement Science and Technology* 32(6):065402.